IEEE Photonics Journal
An IEEE Photonics Society Publication

Sixteen-Pixel NbN Nanowire Single Photon Detector Coupled With 300-μm Fiber

Volume 12, Number 1, February 2020

Qi Chen
Biao Zhang
Labao Zhang
Rui Ge
Ruiying Xu
Yang Wu
Xuecou Tu
Xiaoqing Jia
Danfeng Pan
Lin Kang
Jian Chen
Peiheng Wu

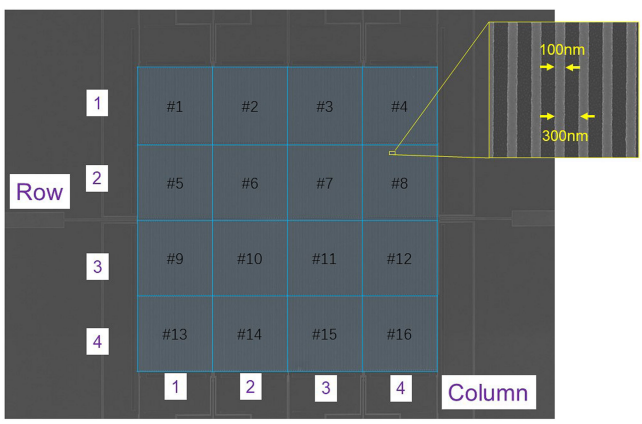

DOI: 10.1109/JPHOT.2019.2954938

Sixteen-Pixel NbN Nanowire Single Photon Detector Coupled With 300-μm Fiber

Qi Chen, Biao Zhang, Labao Zhang, Rui Ge, Ruiying Xu, Yang Wu, Xuecou Tu, Xiaoqing Jia, Danfeng Pan, Lin Kang, Jian Chen, and Peiheng Wu

Research Institute of Superconductor Electronics, Nanjing University, Nanjing 210093, China

DOI:10.1109/JPHOT.2019.2954938

Manuscript received June 27, 2019; accepted November 17, 2019. Date of publication November 21, 2019; date of current version January 7, 2020. This work was supported in part by the National Key R&D Program of China under Grant 2017YFA0304002, in part by the National Natural Science Foundation under Grants 61571217, 61521001, 61801206, and 11227904, in part by the Fundamental Research Funds for the Central Universities, in part by the Priority Academic Program Development of Jiangsu Higher Education Institutions (PAPD), in part by the Recruitment Program for Young Professionals, in part by the Qing Lan Project, and in part by the Jiangsu Provincial Key Laboratory of Advanced Manipulating Technique of Electromagnetic Waves. Corresponding author: Labao Zhang (e-mail: Lzhang@nju.edu.cn).

Abstract: Niobium nitride (NbN) nanowires have a high repetition rate and efficiency, making them ideal for superconducting nanowire single photon detectors (SNSPDs). However, it is difficult to fabricate NbN arrays over large areas, which is critical for various applications. This paper describes a 4 $\times$ 4 NbN SNSPD array (16 pixels) and optical coupling with a 300-μm-diameter multimode fiber using beam compression technology. This is the first NbN SNSPD coupled with such large-diameter fibers. The designed pixels are positioned as closely as possible (pixel filling factor about 98.5%), almost without dead area between them. This results in a system efficiency of 46% and a quantum efficiency of 94.5% for photons ($\lambda = 1064$ nm) coupled from multimode fibers. An intrinsic time resolution of less than 69 ps can be obtained. The proposed high-performance single photon detector is suitable for satellite laser ranging. Furthermore, the proposed system is feasible for large SNSPD arrays with NbN, paving the way for the development of efficient photon cameras with NbN nanowires.

Index Terms: Multimode fiber, niobium nitride, satellite laser ranging, single-photon detector.

1. Introduction

Superconducting nanowire single photon detectors (SNSPDs) have created a revolution in detector performance and scientific applications [1]. Since the first SNSPD, composed of a 1-μm-long, 200-nm-wide nanowire, was reported [2], SNSPDs have reached 93% detection efficiency [3], sub-10 ps time jitter [4], and less than 0.01 cps dark count rate [5]. They have been applied in loop-free tests of the Bell equation [6], [7], lunar-to-earth laser communication [8], [9], quantum imaging [1], [10], linear optical quantum computing [11], and high-speed quantum key distribution [12].

Niobium nitride (NbN) nanowires are typically used in SNSPDs because of their low dark count rate [5], low time jitter [13], high repetition rate [14], and high critical temperature [15] compared

with amorphous materials such as WSi [16] and MoSi [17]. A recent study [18] indicated that NbN-based SNSPDs also deliver excellent performance, achieving efficiency of greater than 90%. Therefore, NbN is a highly promising material for SNSPD research. However, NbN in SNSPDs is a polycrystalline or single-crystal epitaxial material, depending on the substrate. Thus, it is difficult to produce a uniform, high-quality film over a large area because of factors such as the crystal orientation and lattice defects [19].

Over the past decade, increasing the number of NbN-nanowire arrays and the active detection area has received considerable attention. Conventional methods sacrifice the filling factor and reduce the detection efficiency (usually to less than 10%). Doerner *et al.* [20] developed a 16-pixel SNSPD array with a filling factor of just 14%, resulting in a maximum detection efficiency of less than 10%. Divochiy *et al.* [21] proposed a parallel nanowire detector with a low filling factor that achieved a quantum efficiency of only $\sim$2% at 1.3 μm. Jahanmirinejad *et al.* [22] developed a nanowire array that covered a total active area of only 12 μm $\times$ 12 μm, while Miki *et al.* [23] proposed a 64-pixel SNSPD with a filling factor of 40% over an area of 63 μm $\times$ 63 μm. The fabrication of high-efficiency NbN-nanowire arrays requires much higher chip yields. Scientists have concluded that it is difficult to prepare SNSPDs with large active areas using NbN [3], [16].

In this study, an NbN-based SNSPD array consisting of 16 elements is fabricated. The detection area of 80 μm $\times$ 80 μm is arranged in a 4 $\times$ 4 array, with every pixel having the same size of 20 μm $\times$ 20 μm. The designed pixels are positioned as closely as possible (pixel filling factor of about 98.5%), almost without dead area between them. Beam compression technology is adopted during photon coupling, which reduces the difficulty of optical coupling and the photon loss caused by the coupling process. Consequently, a system detection efficiency of 46% and quantum efficiency of 94.5% can be achieved. The detector is known to be a high-performance single photon detector suitable for satellite laser ranging [24], [25]. It demonstrates the feasibility of constructing a large SNSPD array using NbN, and paves the way for the development of high-efficiency photon cameras using NbN nanowires.

2. Experimental

2.1 Device Design

The optimization of the device structure refers to the design of Min *et al.* [26]. The traditional high-Q optical cavity structure is adopted for the SNSPD structural design, and finite difference–time domain software is used to optimize the device structure parameters. Fig. 1(a) depicts the simulation model. The substrate material is Si. To enhance the light absorption rate of the nanowire, a Si_3N_4 anti-reflection film is adopted and a thin layer of Si_3N_4 (thickness 135 nm) is added to the lower layers of the model as a resonator. The nanowires are placed above the lower resonant cavity. To further enhance the light absorption rate of the nanowire, an upper Si_3N_4 resonant cavity is added above the nanowires. Furthermore, a 200-nm-thick gold mirror is prepared on the upper resonant cavity to completely reflect photons. In the structure of the device, both the upper and lower layers of Si_3N_4 form a complete optical cavity. In the simulation process, the cavity structure boundary conditions are set as follows: periodic boundary conditions are set in both the x and y directions, while the z direction is assumed to be a perfectly matched layer. The photons enter the device from the back of the Si substrate, the light is polarized, and the polarization directions are parallel and perpendicular to the nanowires. Combining theory and practice, the nanowire linewidth is 100 nm, the nanowire filling factor is 1/3, and the film thickness is 6.5 nm. To facilitate rapid simulations while obtaining high-precision results, further mesh refinement is conducted on the part of the NbN nanowires. The grid precision in the x, y, and z triaxial directions is set to 0.5 nm. The $x = 0$ plane is simulated with a two-dimensional plane composed of the y-axis. Wavelengths λ ranging from 600–1600 nm are simulated. The refractive index n of each simulated material varies with the wavelength: when $\lambda = 1064$ nm, $n_{\mathrm{Si}} = 3.4215$; $n_{\mathrm{Si3N4}} = 2.0112$; $n_{\mathrm{NbN}} = 4.1141 + 4.9423\mathrm{i}$; $n_{\mathrm{Au}} = 0.28 + 9.03\mathrm{i}$ (obtained by spectroscopic ellipsometer).

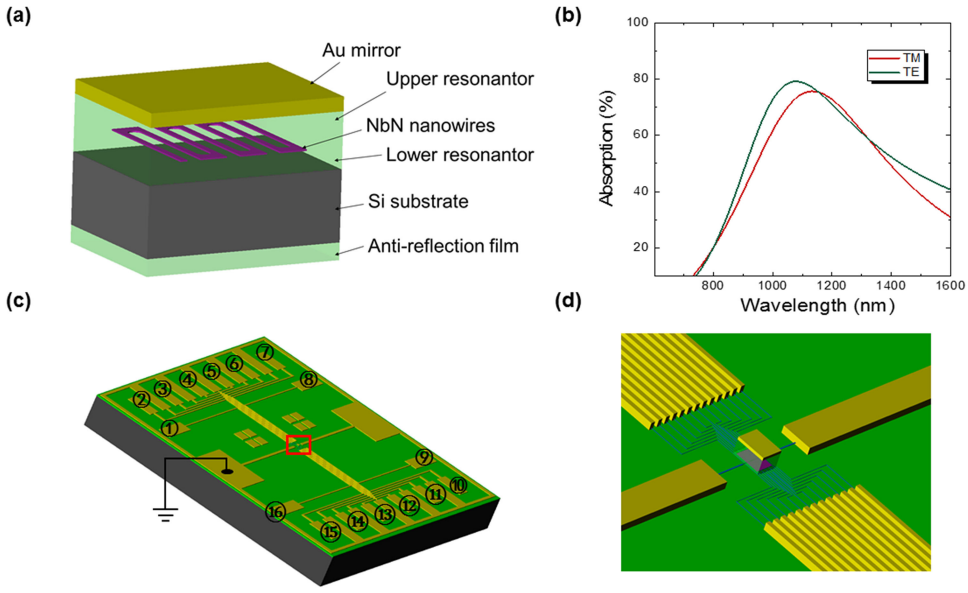

Fig. 1. Device design and simulation diagrams. (a) Simulated structure. (b) Absorption of NbN nanowires vs. wavelength. With changing wavelength, the absorption of TE and TM waves varies. (c) Three-dimensional structure of the SNSPD; red box indicates the detection area of the SNSPD. (d) Magnification of the nanowire detection area, where the purple part represents the nanowire array.

To maximize the absorption rate of photons by NbN nanowires, it is necessary to optimize the thickness d of the upper resonator to achieve critical coupling. This optimization was achieved through a series of simulations. Changing the thickness of the upper resonator also changes the center wavelength. After optimization, a relatively suitable thickness of $d = 133$ nm was obtained. The simulation results are shown in Fig. 1(b). As the wavelength changes, the absorption rate of transverse electric (TE) and transverse magnetic (TM) waves by the NbN nanowires varies. The maximum absorption rate of polarized waves by NbN nanowires is around 70% for TM waves and 79% for TE waves at a wavelength of 1064 nm. The device is insensitive to the polarization of light. Fig. 1(c) shows the three-dimensional structure of the SNSPD. The yellow structure represents an Au electrode. The purple part of Fig. 1(d) represents the nanowire array. An Au mirror is installed above it, and the 16 nanowire pixels are connected to 16 Au short pins. Electrode numbers 1–16 are marked. To facilitate the layout of the nanowire array and the subsequent device test analysis, 10 long pins are designed. Between the 16 Au short pins, there are two large-size pins in the middle of the device. These are designed to connect the G levels of nanowire pixels. The device is connected to a grounded outer frame to achieve a common ground.

2.2 Optimization of the Fabrication Process

In this experiment, a nanowire width of 100 nm was designed with a nanowire filling factor of 1/3. The total active area of the superconducting nanowires was increased to 80 μm $\times$ 80 μm, with each pixel having a size of 20 μm $\times$ 20 μm. Compact wiring between pixels ensured a 98.5% pixel filling rate. For the convenience of the testing and analysis, each pixel number is defined as #1, #2, … in Fig. 2.

The nanowire preparation process was based on previous work [27]–[29]. The materials and micro-nanofabrication processing were optimized as much as possible. First, by optimizing the plasma-enhanced chemical vapor deposition (PECVD) process, the refractive index of Si_3N_4 at $\lambda = 1064$ nm and the surface flatness were optimized to 2.0112 and less than 0.5 nm (root mean square), respectively. As the lower resonator, a 135-nm-thick Si_3N_4 layer was grown on the front of

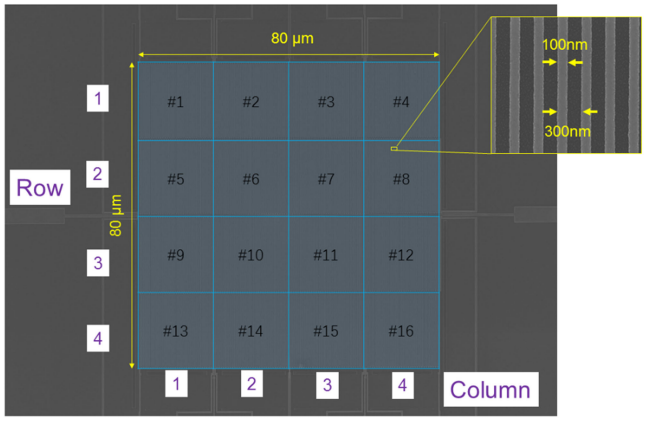

Fig. 2. SEM image of the nanowire array.

the wafer using a Plasma80Plus device (Oxford Instruments) with a growth temperature of 300 °C. To reduce the reflectivity of photons from the back of the device, a 135-nm-thick Si_3N_4 anti-reflection film was also grown. Next, NbN film was deposited on the lower resonator via DC magnetron sputtering (model number DE500). The NbN film had a thickness of 6.5 nm and a superconducting critical temperature of 8.3 K. The Au electrode was prepared via photolithography (the Au electrode can achieve low transmission loss of the RF signal, and can also help to adjust the incident beam to the device detection area during the packaging process). A two-layer adhesive lithography process was used. The lower layer of the glue was LOR10B and the upper layer was AZ1500. The Au electrode was grown via DC magnetron sputtering (model number DE500). The Au thickness was ∼200 nm. To enhance the adhesion of the Au electrode to the NbN, a Ti film (10-nm thickness) was grown between the Au and NbN. After the lift-off process, the Au electrode was fully prepared and electron beam exposure could commence.

The substrate was spin-coated with a 2% concentration of hydrogen silsesquioxane (HSQ), which is an electron beam photoresist (Dow Corning Co.) [30]. The spinner rotation speed was controlled to ∼5000 rpm and the spin coating time was 1 min. After spin coating had been completed, the substrate was baked on a drying table at 100 °C for 3 min. After baking, the substrate was left to return to room temperature before being subjected to electron beam lithography (EBPG5200, Raith). During the electron beam lithography process, the electron beam current was set to 0.2 nA and the acceleration voltage was 100 kV. These values were chosen to ensure excellent quality nanowires with a reasonable exposure time. In addition, as the electron proximity effect is particularly severe during large-area exposure, reasonable control of the exposure dose is important. Fig. 3 shows the relationship between the exposure dosage and nanowire linewidth during electron beam lithography, with dosages ranging from 1100–1800 μC/cm^2.

For the convenience of analysis, four pixels (1, 6, 11, and 16) were selected. Fig. 3(a) shows the different nanowire linewidths and standard deviations for these four pixels at different exposure dosages. Nanowires obtained in pixels 1 and 16, or in pixels 6 and 11, at the same exposure dosage have the same linewidth. This indicates that the electron beam lithography at different positions is consistent without considering the electron beam proximity effect. Moreover, due to the electron beam proximity effect, the nanowire width in pixels 6 and 11 exceeds the edge portions of pixels 1 and 16 to different extents for different exposure dosages. When the exposure dosage is too high, the width uniformity of the nanowires decreases, which is detrimental to their preparation. Fig. 3(b) shows the extent to which the width of the nanowires obtained under different exposure dosages deviates from the theoretically predicted value. This deviation factor (DF) can be calculated as:

$$DF_{100} = \left(\frac{|W_{max} - 100|}{100} + \frac{|W_{min} - 100|}{100} \right) \times 100\% \quad (1)$$

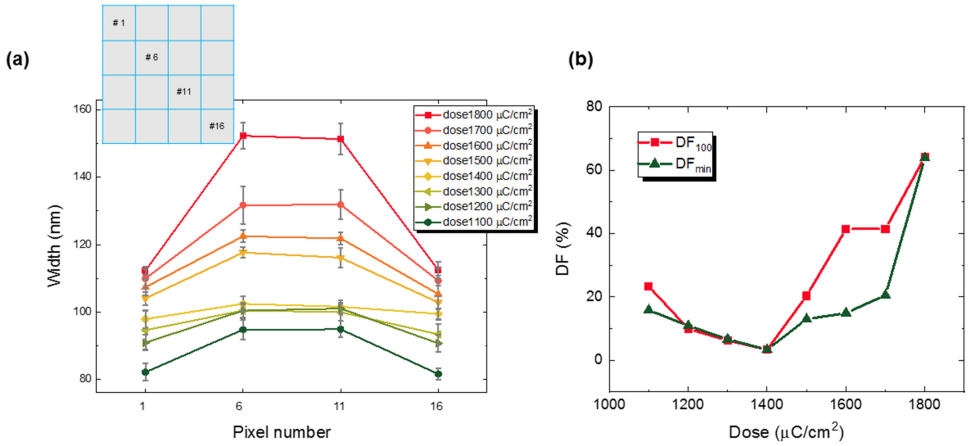

Fig. 3. (a) Inset shows pixels 1, 6, 11, and 16, which were selected for the experiment. Nanowire linewidth and deviation for the four pixels change as the dosage varies from 1100–1800 μC/cm^2. (b) Red line shows the total deviation percentage of the maximum and minimum nanowire linewidths from the design values of 100 nm at different exposure dosages. Green line shows the percentage difference between the minimum and maximum nanowire linewidths at different exposure dosages.

$$\mathrm{DF}_{\min} = \left(\frac{W_{\max} - W_{\min}}{W_{\min}}\right) \times 100\% \tag{2}$$

where DF_{100} represents the total percentage of the maximum linewidth and the minimum linewidth offset of the design values of 100 nm for a specific exposure dosage, reflecting both theoretical and practical consistency. $\mathrm{DF}_{\min}$ denotes the percentage difference between the maximum and minimum linewidths at a specific exposure dosage, indicating the uniformity of the nanowire. $W_{\max}$ and $W_{\min}$ represent the maximum and minimum linewidths, respectively. Figs. 3(a) and 3(b) show that the linewidths of the four pixels are around 100 nm at a dosage of 1400 μC/cm^2. It is also clear that the proximity effect is relatively weak and both DF_{100} and $\mathrm{DF}_{\min}$ are minimized, indicating ideal exposure. The dosage was therefore set to 1400 μ/cm^2 in the electron beam lithography processing. After the nanowire pattern had formed, it was developed through a ZX-238-type HSQ developer at room temperature. The optimized development time was 2.5 min. The NbN nanowires were then obtained using reactive ion etching apparatus (RIE-10, SAMCO). SF_6 and CHF_3 with flow rates of 40 sccm and 10 sccm, respectively, were used as etching gases. The gas pressure was set to 4 Pa, the power was set to 100 W, and the etching time was 20 s.

After preparation of the nanowire array, similar to the growth of the lower resonator, the upper Si_3N_4 optical cavity was grown by PECVD. Similar to the growth of the Au electrode, an Au mirror was grown via DC magnetron sputtering. The superconducting nanowires of all pixels were connected to the corresponding electrodes, and the electrodes were connected to the RF connectors.

3. Results and Analysis

3.1 Measurement Settings

As shown in Fig. 4(a), a dedicated package and opto-light platform were designed for the SNSPD, with one pin of the 16 pixels grounded and the other end directed to the SMA port. A dual-aspheric lens system was used to focus the light beam from the multimode fiber onto the active area of the SNSPD. Fig. 4(b) shows a schematic diagram of the signal processing in the experiment. D_1, D_2, ..., D_{15}, and D_{16} represent mutually independent pixels, A_1, A_2, ..., A_{15}, and A_{16} represent 16 identical low-noise power amplifiers. A ps-pulse laser with an output light wavelength of $\lambda =$ 1064 nm was adopted. The frequency of the laser could be adjusted from 1–100 MHz. Photons

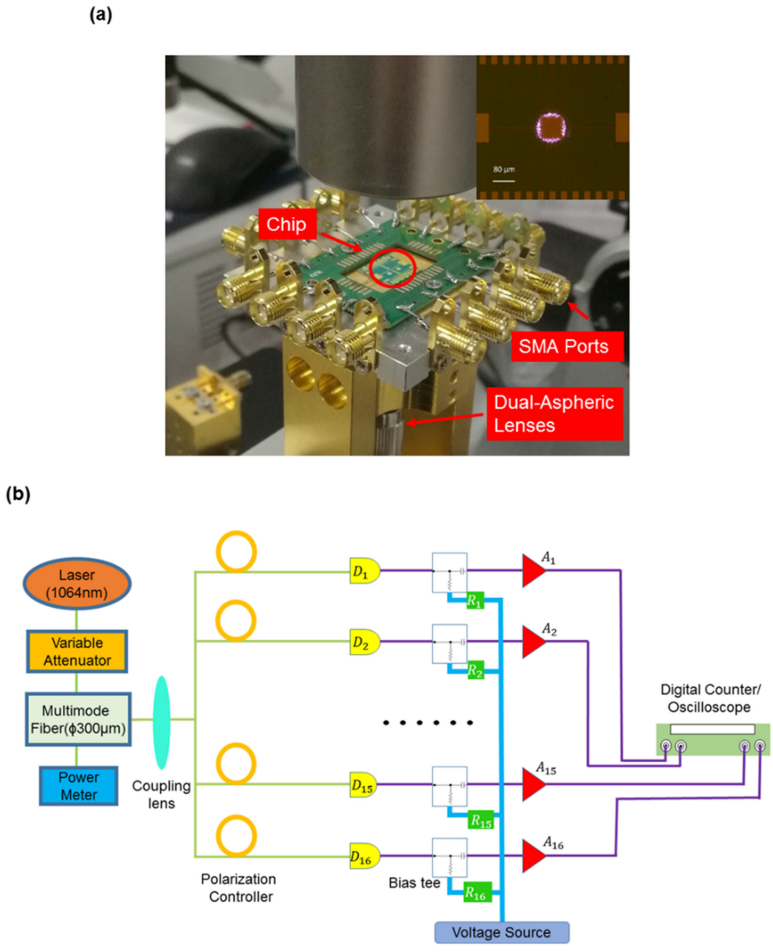

Fig. 4. (a) Dedicated package and opto-light platform designed for the SNSPD, with one pin of 16 pixels grounded and the other end directed to the SMA port. Inset taken through an optical microscope shows the detection area illuminated by the compressed beam with a diameter of ∼100 μm. (b) Schematic diagram of the signal processing for SNSPD.

emitted by the laser were attenuated by a variable attenuator and then coupled onto the detection area using beam compression technology. A polarization controller was adopted to adjust the polarization of the beam and obtain the highest detection efficiency.

Based on previous work [31], [32], a beam compression system with two aspheric lenses was coupled to the multimode fiber to compress the optical beam with a magnification factor of ∼1/3. The numerical apertures (NA) of the multimode fiber and the dual-lens system were ∼0.22 and ∼0.66, respectively. The magnification factor was ∼1/3. Thus, the imaging size (focused beam) was estimated at 100 μm in diameter for the core (diameter: ∼300 μm) of the multimode fiber, similar to a Gaussian spot. A nominal coupling efficiency (the calculation principle was also introduced in the previous studies) of 95 $\pm$ 2% can be obtained by chips with a detection area of 80 μm $\times$ 80 μm.

The output signal of the SNSPD was amplified by a low-noise amplifier. Finally, all pulses from each pixel were collected, displayed via a real-time oscilloscope, and analyzed with a digital counter. All optical components in the system were fiber-optic, and all electrical components were connected via coaxial cable.

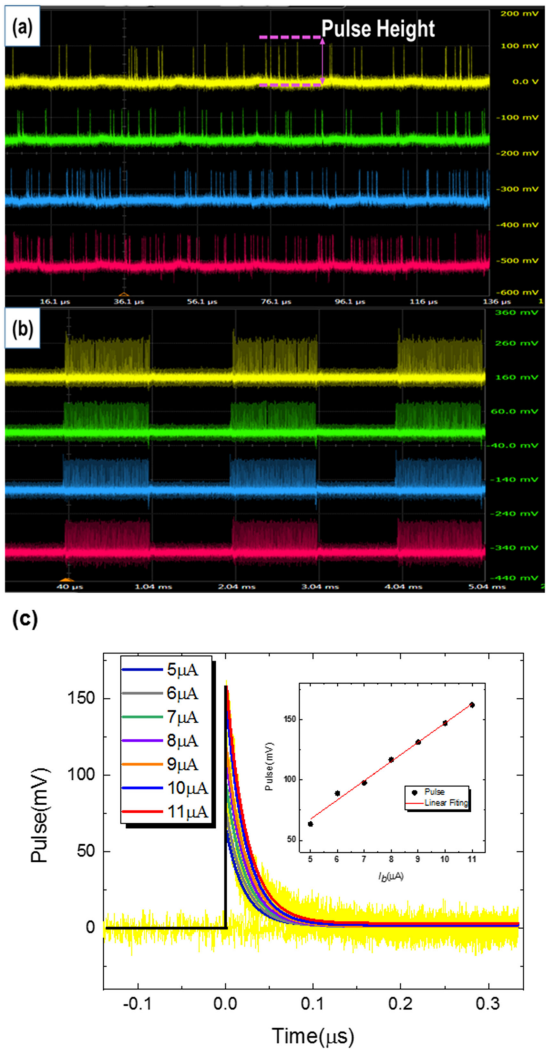

Fig. 5. Output signal generated by four arbitrarily selected channels. (a) Random distribution of the electrical pulse in run-free mode. (b) Electrical pulse signal in quasi-gated mode. (c) Voltage pulse exponential fitting curve for different bias currents. Inset shows linear relationship between V_p and I_b.

3.2 Consistency Analysis

The average resistance of the 16 ports in the array device, measured at room temperature, was 4.04 MΩ with a relative standard deviation of 3.7%. The device resistance was evenly distributed. The device was mounted on a compacted G-M cryocooler and cooled to 2.2 K. The mean value of the superconducting critical current I_c of each pixel was 11.63 μA with a relative standard deviation of 6.9%.

A high-speed oscilloscope collected all electrical pulse signals generated by the nanowires after photon absorption when the system was in operation. Fig. 5(a) shows the random distribution of the electrical pulses in run-free mode. There is a low signal-to-noise ratio. Fig. 5(b) shows the random distribution of the electrical pulse signals recorded by the oscilloscope over an extended period of time using a gated method. A comparison shows that the amplitudes of the electrical pulse signals generated by the same pixel at different times are generally identical; furthermore, the amplitudes of the electrical pulse signals generated by different pixels are similar. This shows that the performance of all pixels is consistent and the system is stable. Fig. 5(c) shows the voltage

pulses and the exponential fitting curves under different bias currents. The fitting equation is:

$$y = y_0 + Ae^{-\frac{t}{\tau}} \tag{3}$$

The average reset time τ of six-time fitting is 20.25 ns, and the resistance R is 50 Ω. According to Eq. (3) with $\tau = Lk/R$, the kinetic inductance L_k of the nanowire is $\sim$1 μH.

The bias current I_b affects the amplitude V_p of the output voltage pulse. Pulses of different amplitudes can be obtained by adjusting the bias current, and the V_p–I_b relationship is shown in the inset of Fig. 5(c). The linear fitting curve indicates the high performance of the high-speed oscilloscope.

3.3 Efficiency and Dark Count

A pulsed laser was used to generate pulsed light at $\lambda = 1064$ nm, with each pulse containing an average of one photon. As the experiment used a multimode fiber with a large spot size, the light intensity distribution covered all pixels of the array device. Each pixel was dependently biased in the experiment. Fig. 6 shows the system detection efficiency (SDE) and dark count rate (DCR) in an ultra-low-temperature environment of 2.2 K. Here, a logarithmic scale is adopted to describe the relationship, similar to [33]. The SDE is defined as the ratio of the number of photons measured for each pixel to the total number of incident photons by considering the light coupling loss. The DCR refers to electric pulse signals caused by the SNSPD system without a photon-reaction, resulting in an abnormal count that cannot be distinguished from the normal photon response. Fig. 6(a) shows that SDE increases as the bias current I_b increases up to the switching current. The total detection efficiency is defined as the sum of SDE of each pixel, as measured at the bias current when DCR = 1000 cps. Consequently, the total detection efficiency reached 46%. The SDE distribution of all 16 pixels is shown in the inset. The pixels in the center of the array have the highest efficiency, whereas those in the corners have the lowest efficiency. Therefore, the spot is well-aligned, and matches the inset of Fig. 4(a). The increased count near the switching current may be caused by the DCR. As shown in Fig. 6(b), the DCR is always higher than 1000 cps. In a multimode fiber coupled system, this may be because of the increased background, model dispersion and blackbody radiation during transmission and coupling. In the future, the adoption of a filter is a valid method to solve the problem [5], [34].

The quantum efficiency (QE) expresses the intrinsic efficiency of nanowires, reflecting the probability that a nanowire will generate and output an electric pulse in response to absorbing one photon. Regardless of other secondary factors, QE is characterized as:

$$\mathrm{QE} = \frac{SDE_{\mathrm{total}}}{\alpha_0 (1 - \alpha_l) \eta_a \eta_c} \tag{4}$$

SDE_{total} represents the total detection efficiency as mentioned above. Similar to [3], the uncertainty on the value of SDE_{total} at the operation wavelength (1064 nm) is due to the uncertainty of the number of the incident photons. Here, we estimated the confidence probability of $SDE_{\mathrm{total}} = (46 \pm 4\%)$. where α_0, α_l, η_a, and η_c represent the transmittance of light through the silicon substrate, loss rate of light in the multimode fiber, absorption efficiency of photons by nanowires, and coupling efficiency of multimode fibers, respectively. $\alpha_0 = 71.1\%$ was measured via transmission spectrometry, $\alpha_l = 8.8\%$ was obtained through measurements of the multimode fiber. Both values had similar uncertainties, which were below 1%. $SDE_{\mathrm{total}} = 46\%$ related to η_a reached the maximum value (79%), and the uncertainty on η_a remained below 1%. $\eta_c = 95 \pm 2\%$ was obtained earlier. Thus, the confidence probability of QE was calculated as $94.5 \pm 4.5\%$. This high QE demonstrated the high photoelectric conversion efficiency of the nanowires.

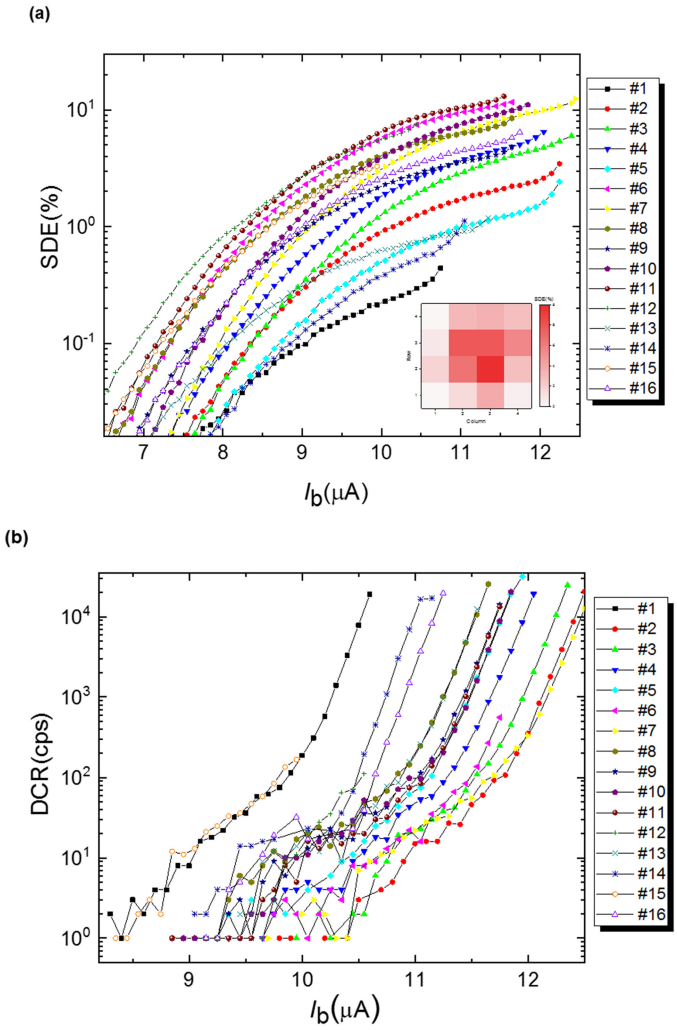

Fig. 6. System detection efficiency (SDE) and dark count rate (DCR) tested in an ultra-low-temperature environment of 2.2 K. (a) Experimental results for SDE. Inset shows the SDE distribution of 16 pixels under a bias current when DCR = 1000 cps. (b) Experimental results for the dark count rate.

3.4 Time Jitter

Time jitter is generally defined as the difference between the actual and the ideal arrival time of photons, or as the deviation in the interval between the rising edges of the electrical pulse signal generated by the single photon response and the theoretically predicted value at which the pulse optical frequency remains constant. The basic measurement system for this experiment is illustrated in Fig. 7(a). A mode-locked femtosecond laser with a wavelength of 1550 nm was used. Jitter caused by the light pulse time distribution would be negligible, as the light pulse is very thin. Furthermore, with a short fiber (a few meters long), the pulse broadening caused by dispersion could be ignored. The output light was split into two paths through the splitter, one of which could only be detected by a low-jitter fast diode, which provides a reference time signal for the high-speed oscilloscope. The other was the input signal of the SNSPD through the attenuator. Power synthesis [29] was used to superimpose the response pulse signals from all channels, and the result was then output on the high-speed oscilloscope. A multimode fiber was used to measure the integrated time jitter. The time jitter can be calculated by measuring the distribution of the delay (Δt) between the SNSPD response pulse and the reference pulse.

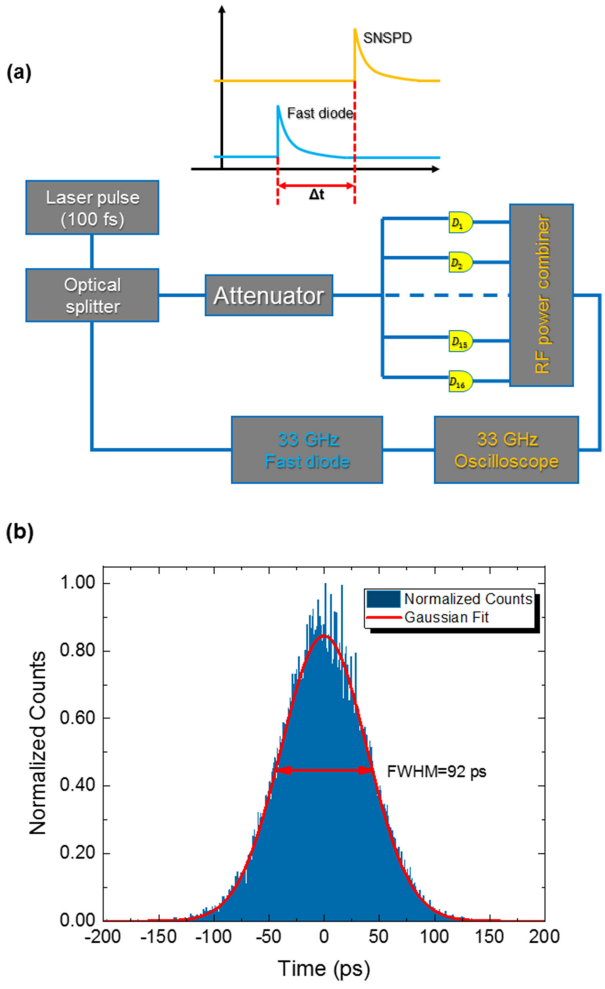

Fig. 7. (a) Time jitter measurement diagram. (b) Blue histogram shows the normalized counts of photons, and the red curve shows the Gaussian fit of the experimental data.

The time jitter is given by:

$$J_{\text{total}} = \sqrt{J_n^2 + J_0^2 + J_{intrinsic}^2 + J_{cd}^2} \tag{5}$$

where J_{total} represents the integrated time jitter; J_n represents the time jitter generated by the circuit part; J_0 represents the inherent time jitter of the high-speed oscilloscope ($J_0 \leq 0.5$ ps); $J_{intrinsic}$ represents the intrinsic time jitter of the array device, which not only contains the intrinsic time jitter of each pixel but also an additional time jitter caused by mutual interference between pixels; and J_{cd} represents the time jitter generated by the light source and the optical path, which is related to the source bandwidth, dispersion coefficient, and transmission fiber. Generally, this is a sub-ps delay. According to the linear small model perturbation theory and a previous publication [17], J_n can be computed as:

$$J_n = \frac{\sigma_n}{k} \times 2\sqrt{2ln2} \tag{6}$$

where σ_n and k represent the root mean square of the circuit noise and the slope of the rising edge of the response signal at the discrimination level, respectively. The magnitude of σ_n is determined via the amplitude of the noise signal, whereas k is affected by the rising edge time of the pulse

signal, the magnitude of the bias current, the gain of the amplifier, and the response bandwidth. In Fig. 7(b), the blue histogram shows the normalized count rate of photons and the red curve shows the Gaussian fit of the experimental data. J_{total} is ~92 ps at the bias currents with DCR = 1000 cps of all pixels. According to statistical analysis, the magnitude of σ_n is 5.077 mV, and the value of k is 196 mV/ns, resulting in $J_n = 61$ ps. According to Eq. (5), $J_{intrinsic} < 69$ ps.

4. Conclusion

In summary, this study proposed and fabricated a novel multi-pixel SNSPD with large detection area, high pixel filling factor, and high detection efficiency for the first time. The developed 4×4 array consists of 16 compactly arranged pixels, each of which with a size of 20 μm $\times$ 20 μm, yielding a total active area of 80 μm $\times$ 80 μm. A multimode fiber with a diameter of up to 300 μm was introduced into the optical path via beam compression technology, greatly reducing the difficulty of optical coupling and the photon loss caused by this coupling process. The photon absorption efficiency is insensitive to the polarization state of light. Loss caused by the unpredictable polarization state of the optical signal can be avoided when the device is used for space detection. The relationship between the exposure dosage and the nanowire linewidth during electron beam exposure was clarified through a series of experiments, and the optimized dosage condition was determined. The experimental results show that the SDE of the SNSPD reaches 46%, with QE of 94.5% at $\lambda = 1064$ nm without optimizing polarization, indicating the high photoelectric conversion efficiency of the nanowire. An intrinsic time resolution of less than 69 ps can be obtained. The detector has already demonstrated its ability as a high-performance single photon detector for the satellite laser ranging application. Furthermore, this study demonstrates the feasibility of a large SNSPD array, and paves the way for the development of efficient photon cameras with NbN nanowires. However, it will meet further challenges when larger array and larger areas are required. For example, good homogeneity of nanowires cannot be guaranteed during the nano-fabrication process due to the electron proximity effect. Furthermore, the filling factor between pixels will decrease due to the nano-circuit structure of pixels, thus lowering the detection efficiency. The introduction of a micro-lens array is an effective way to solve the problem.

Acknowledgment

Disclosure: The authors declare that they have no competing interests.

Author Contributions Statement: L. Z. conceived the experiment. Q. C., R. X., X. T., D. P., X. J., L. K., and L. Z. designed and fabricated the SNSPD device. B. Z., R. G., Y. W., J. C., P. W., and L. Z. characterized the device and system of SNSPDs. L. Z., Q. C., and B. Z. analyzed the data and prepared all figures. L. Z., Q. C., and B. Z. wrote the manuscript. All authors discussed the results and commented on the manuscript.

References

[1] D. Shin *et al.*, "Photon-efficient imaging with a single-photon camera," *Nat. Commun.*, vol. 7, 2016, Art. no. 12046.
[2] G. N. Gol'tsman *et al.*, "Picosecond superconducting single-photon optical detector," *Appl. Phys. Lett.*, vol. 79, pp. 705–707, 2001.
[3] F. Marsili *et al.*, "Detecting single infrared photons with 93% system efficiency," *Nat. Photon.*, vol. 7, pp. 210–214, 2013.
[4] I. E. Zadeh *et al.*, "A single-photon detector with high efficiency and sub-10ps time resolution," 2018. [Online]. Available: https://arxiv.org/abs/1801.06574.
[5] H. Shibata, K. Fukao, N. Kirigane, S. Karimoto, and H. Yamamoto, "SNSPD with ultimate low system dark count rate using various cold filters," *IEEE Trans. Appl. Supercond.*, vol. 27, no. 4, Jun. 2017, Art. no. 2200504.
[6] L. K. Shalm *et al.*, "Strong loophole-free test of local realism," *Phys. Rev. Lett.*, vol. 115, 2015, Art. no. 250402.
[7] M. Giustina *et al.*, "Significant-loophole-free test of bell's theorem with entangled photons," *Phys. Rev. Lett.*, vol. 115, 2015, Art. no. 250401.
[8] M. E. Grein *et al.*, "Design of a ground-based optical receiver for the lunar laser communications demonstration," in *Proc. Int. Conf. Space Opt. Syst. Appl.*, 2011, pp. 78–82.
[9] M. E. Grein *et al.*, "A fiber-coupled photon-counting optical receiver based on NbN superconducting nanowires for the lunar laser communication demonstration," in *Proc. Conf. Lasers Electro-Opt.*, San Jose, CA, USA, 2014, SM4J.5.

[10] A. Kirmani *et al.*, "First-photon imaging," *Science*, vol. 343, no, 6166, pp. 58–61, Jan. 2014.
[11] N. K. Langford *et al.*, "Efficient quantum computing using coherent photon conversion," *Nature*, vol. 478, pp. 360–363, 2011.
[12] N. Sangouard *et al.*, "Long-distance entanglement distribution with single-photon sources," *Phys. Rev. A*, vol. 71, 2007, Art. no. 050301.
[13] J. Wu *et al.*, "Improving the timing jitter of a superconducting nanowire single-photon detection system," *Appl. Opt.*, vol. 56, pp. 2195–2200, 2017.
[14] D. F. Santavicca, "Prospects for faster, higher-temperature superconducting nanowire single-photon detectors," *Supercond. Sci. Technol.*, vol. 31, 2018, Art. no. 040502.
[15] A. Semenov *et al.*, "Optical and transport properties of ultrathin NbN films and nanostructures," *Phys. Rev. B*, vol. 80, 2009.
[16] J. P. Allmaras *et al.*, "Large-area 64-pixel array of WSi superconducting nanowire single photon detectors," in *Proc. Conf. Lasers Electro-Opt.*, San Jose, CA, USA, 2017, JTh3E.7.
[17] M. Caloz *et al.*, "High-detection efficiency and low-timing jitter with amorphous superconducting nanowire single-photon detectors," *Appl. Phys. Lett.*, vol. 112, 2018, Art. no. 061103.
[18] W. J. Zhang *et al.*, "NbN superconducting nanowire single photon detector with efficiency over 90% at 1550 nm wavelength operational at compact cryocooler temperature," *Sci. China Phys., Mech. Astron.*, vol. 60, pp. 1674–7348, 2017.
[19] A. J. Kerman *et al.*, "Constriction-limited detection efficiency of superconducting nanowire single-photon detectors," *Appl. Phys. Lett.*, vol. 90, 2007, Art. no. 101110.
[20] S. Doerner *et al.*, "Frequency-multiplexed bias and readout of a 16-pixel superconducting nanowire single-photon detector array," *Appl. Phys. Lett.*, vol. 111, 2017, Art. no. 032603.
[21] A. Divochiy *et al.*, "Superconducting nanowire photon-number-resolving detector at telecommunication wavelengths," *Nat. Photon.*, vol. 2, pp. 302–306, 2008.
[22] S. Jahanmirinejad *et al.*, "Photon-number resolving detector based on a series array of superconducting nanowires," *Appl. Phys. Lett.*, vol. 101, 2012, Art. no. 072602.
[23] S. Miki *et al.*, "Large sensitive-area NbN nanowire superconducting single-photon detectors fabricated on single-crystal MgO substrates," *Appl. Phys. Lett.*, vol. 92, 2008, Art. no. 061116.
[24] L. I. Xue *et al.*, "Satellite laser ranging using superconducting nanowire single-photon detectors at 1064 nm wavelength," *Opt. Lett.*, vol. 41, pp. 3848–3851, 2016.
[25] R. U. Tang *et al.*, "Light curve measurements with a superconducting nanowire single-photon detector," *Opt. Lett.*, vol. 43, pp. 5488–5491, 2018.
[26] M. Gu *et al.*, "High efficiency, large-active-area superconducting nanowire single-photon detectors," *Chin. Phys. B*, vol. 24, 2015, Art. no. 068501.
[27] L. Zhang *et al.*, "Maximizing switching current of superconductor nanowires via improved impedance matching," *Appl. Phys. Lett.*, vol. 110, 2017, Art. no. 072602.
[28] L. Zhao *et al.*, "Single photon detectors based on superconducting nanowires over large active areas," *Appl. Phys. B-Lasers Opt.*, vol. 97, pp. 187–191, 2009.
[29] L. Zhang *et al.*, "A multi-functional superconductor single-photon detector at telecommunication wavelength," *Appl. Phys. B Lasers Opt.*, vol. 115, pp. 295–301, 2014.
[30] Y. Chen *et al.*, "Effects of developing conditions on the contrast and sensitivity of hydrogen silsesquioxane," *Microelectron. Eng.*, vol. 83, pp. 1119–1123, 2006.
[31] L. Zhang *et al.*, "Dual-lens beam compression for optical coupling in superconducting nanowire single-photon detectors," *Sci. Bull.*, vol. 60, pp. 1434–1438, 2015.
[32] L. Zhang *et al.*, "Multimode fiber coupled superconductor nanowire single-photon detector," *IEEE Photon. J.*, vol. 6, no. 5, Oct. 2014, Art. no. 6802608.
[33] S. Miki *et al.*, "A 64-pixel NbTiN superconducting nanowire single-photon detector array for spatially resolved photon detection," *Opt. Exp.*, vol. 22, pp. 223–225, 2014.
[34] W. J. Zhang *et al.*, "Fiber-coupled superconducting nanowire single-photon detectors integrated with a bandpass filter on the fiber end-face," *Supercond. Sci. Technol.*, vol. 31, 2018, Art. no. 035012.